Effect of nano-Cr_2O_3 on W-Zr alloys mechanical properties

Bappa Das[*], A. Patra

Department of Metallurgical and Materials Engineering, National Institute of Technology, Rourkela-769008, India
Corresponding author's email ID: bappa123.2011@gmail.com

Abstract

Tungsten alloys with the nominal compositions of $W_{98.5}Zr_{0.5}(Cr_2O_3)_1$(alloy A), $W_{97.5}Zr_{0.5}(Cr_2O_3)_2$ (alloy B) and $W_{98}Zr_1(Cr_2O_3)_{(1)}$ (alloy C) (weight %) were fabricated. The properties were investigated by XRD, SEM, EDS and Elemental mapping. Differential Scanning Calorimetric (DSC) of the 20 h milled powder in argon atmosphere has been carried out at heating rate (10 K/min) up to 1273 K (1000°C). Excellent powder flowability was found in alloy A. Alloy C has the higher dispersion stability. The smallest particle size of 321.6nm observed in Alloy C at 20 h was measured using DLS.

Keywords: Tungsten based alloys; Mechanical alloying; X- ray diffraction; Scanning electron microscope; Particle size; Flowability; Zeta potential.

1. Introduction

Tungsten is one of the promising worldwide refractory material for elevated temperature applications in electrical, fusion reactor, electronics, defense, space aviation counterweights technologies because of its high melting point (3410 °C), impressive hardness of 9.8 GPa, highest density (19 g/cm^3), thermal conductivity (155 W/m. K at 20 °C), elastic modulus (411 GPa at 20 °C) as well the low vapor pressure [1]. Nanocryastalline and Amorphous tungsten alloys due to its high yield strength, high hardness and better mechanical properties gained excellent demand in recent years. Mechanical alloying for synthesis of tungsten based alloys provides microstructural refinement and average particle size reduction as compared to rapid quenching, severe plastic deformation (SPD) [2, 3].

However tungsten and its alloys applications are limited due to exhibiting serious embrittlement in many aspects, i.e. recrystallization brittleness and irradiation induced brittleness[4-6], high ductile brittle transition temperature (DBTT) (200-500 °C) and lower oxidation resistance at moderate temperature with the formation of volatile WO_3 [7]. Low ductility of tungsten alloys is due to sensitivity towards impurities like O, N and P, which segregate on the grain boundaries (GBs) leading to decrement in GBs cohesion. Therefore,

methods that modify impurities distribution at the GBs and strengthen GBs would be effective in increasing the toughness and the strength and ductility. Reducing these impurities via vacuum and zone melting may decrease the DBTT to about 200 °C [8-11]. However, pure W has low high-temperature strength and undergoes recrystallization at comparatively low temperature (~1200 °C) which further reduces the fracture toughness [12]. Ultrafine-grained W due to severe plastic deformation during milling showed improvement in mechanical properties due to decrement of impurities at the GBs [9, 10]. Nevertheless, the large volume fraction of GBs also have major problems at elevated temperature. To increases the creep resistance, stability and high temperature strength, small amount of oxide nano-particles like La_2O_3, Y_2O_3, CeO_2 and Cr_2O_3 dispersed in the tungsten [13-18]. However, with increase in strength there is a decrease in ductility. Micro-alloying elements like titanium (Ti), hafnium (Hf) and zirconium (Zr) can getter oxygen and nitrogen impurities at the GBs and thus significantly enhance the GBs cohesive strength [19, 20]. Therefore, a method which provides combined advantages of GB strengthening and oxide dispersion strengthening at high temperature would be very attractive. Present investigation aims at W-based alloys by making the powders nanostructured by mechanically milling (MA) as well as study the dual effect of Zr and Cr_2O_3 addition on microstructure, evolution of phases and thermal behavior.

2. Materials and method

Elemental tungsten (W) powders (≥ 99.9 % purity, 0.6-1 μm particle size, sigma Aldrich), Zirconium (Zr) powder (-325 mesh or 44 μm particle size) and chromium oxide (Cr_2O_3) powder (98% purity, <100 nm particle size, sigma Aldrich) were milled in high energy planetary ball mill (Fritsch Pulverisette P-5) for 20 h. The ball to powder weight ratio and mill speed of 10:1 and 300 r.p.m. respectively maintained throughout. To minimize the chances of contamination from grinding media or oxidation from environment process control agent (PCA) Toluene was used. The milled powders 1, 5, 10, 15, 20 h were taken out for further characterization purpose. Table. 1 shows the chemical compositions of the powder subjected to mechanical alloying for the study.

Table 1.

Details of the nominal composition selected for the study.

Alloy Name	Chemical composition of alloys [wt.%]		
	W	Zr	Cr_2O_3
A	98.5	0.5	1
B	97.5	0.5	2
C	98.0	1.0	1

The X-ray diffraction pattern (XRD) of the mechanically alloyed milled powders at different stages is investigated by high resolution X-ray diffractometer BRUKER using Co kα radiation (λ=1.79Å). The record has been matched with the JCPDS data bank to route the evaluation of phases during mechanical alloying [21]. The crystallite size and the lattice strain in the mechanically milled with increment time is assessed from the peak broadening and corresponding peak position of the X-ray diffraction pattern [22]. Precise lattice parameter has been calculation from X-ray diffraction pattern with the help of lattice parameter calculated method [22]. The dislocation density induced in the milled powder has been calculated from the following equation as below:

$$\rho = 2\sqrt{3}\frac{(\varepsilon^2)^{1/2}}{D \times b} \qquad (1)$$

Where, b is the burgers vector of dislocations, b= (a√3)/2 for the bcc structure, a = lattice structure, D = crystallite size, ε = lattice strain [23-25].

The morphology of mechanically milled powders has been determined by scanning electron microscopy (JEOL, JSM-6084LV) and the elements presents in the powders are confirmed by energy-dispersive spectroscope (EDS) analysis.

A small amount of mechanically milled powders (approximately 0.05g) has been dispersed in de-ionized water (2 ml) by ultrasonication for about 1 min each to prepare the desired suspension. The pH of the suspension was controlled by using ammonium hydroxide. The formed dispersions was analyzed by Nano-zeta meter to calculate the particle size and to analyze the stability of suspensions at a particular pH value by measuring zeta potential.

3. Results and discussion

3.1 Characterization of W-Zr-Cr$_2$O$_3$ particles

3.1.1. X-ray diffraction (XRD) analysis of milled powder

The XRD pattern of alloy A through C is presented in fig. 1 (a-c) of alloys powder subjected to milling at 0 to 20 h. Fig.1 (a-c) indicates that the intensity of Zr and Cr$_2$O$_3$ diffraction peak is very weaker then W diffraction peaks owning to lower content of them. Fig.1 (a) shows the small intensity of Zr and Cr$_2$O$_3$ at 0 h milling which almost disappears at 20 h of milling (too flat to detect), which confirms the incorporation of them into W lattice. It is also evident from the fig. 1(a-c) that after 20 h of milling, W-Zr-Cr$_2$O$_3$ and W-Cr$_2$O$_3$ alloys had formed. Refinement of the crystallite size of W in increasing milling from 0 to 20 h is evident from the continuous decreases in intensity and broadening of diffraction peak. Formation of lattice defects and refinement in grain size is due to flattening and fragmentation of milled powder

particles leads to broadening of the peak with increasing milling time.
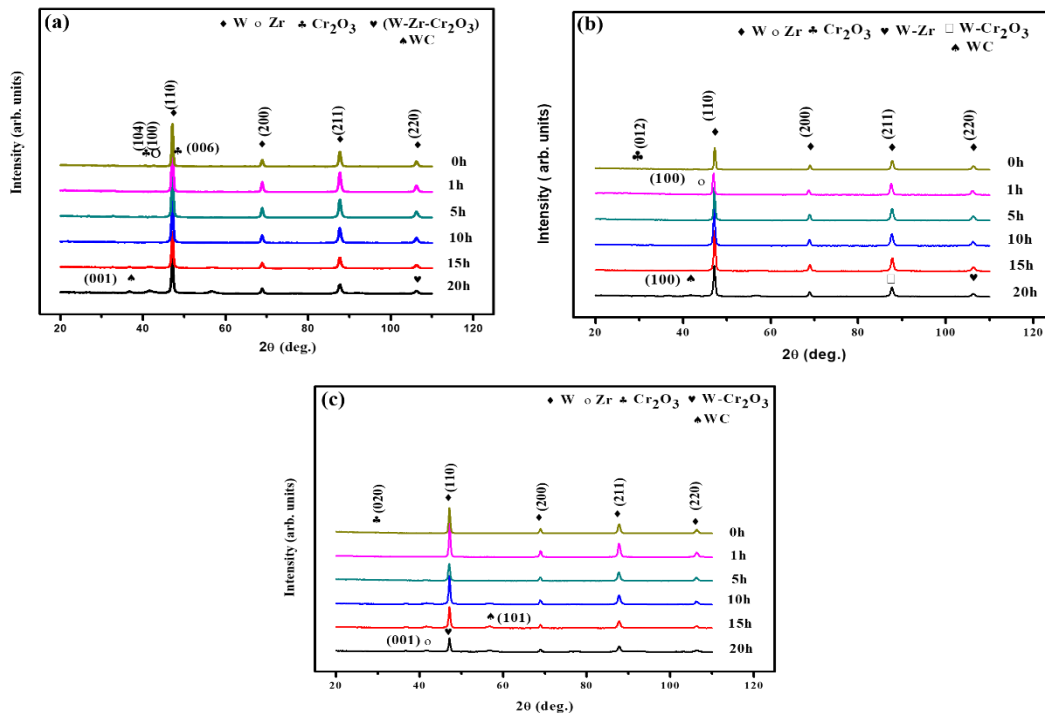

Fig. 1. XRD pattern of mechanically alloyed powder of (a) alloy A, (b) alloy B and (c) alloy C for different milling time.

3.1.2 Crystallite size and lattice strain analysis.

The crystallite size and lattice parameter is evaluated by using Williamson-Hall equation [26] as:

$$\beta \cos\theta = \frac{.94\,\lambda}{D} + 4\eta\,\sin\theta \qquad (2)$$

Where, β is the full width half maxima (FWHM) (broadening), D= crystallite size and η is the lattice strain.

By plotting $\sin\theta$ in x-axis and $\beta \cos\theta$ in y-axis linearly the crystallite size and lattice strain is calculated respectively.

Fig. 2(a) and (b) shows the crystallite size and the lattice strain of the mechanically milled powders with increase in milling time respectively for alloy A through C. It is evident that reduction in the crystallite size and plastic strain buildup is resulted from the increment of (FWHM) broadening with increasing milling time. Minimum crystallite size of 11.8 nm and the maximum lattice strain of 0.44% was achieved in alloy A at 20 h milling time due to presence of high surface energy associated with dispersed Cr_2O_3 particles which are in nanometer. Reduction rate of crystallite size at initial 10 h of milling is high as compared to

milling time beyond 10 h. The stress required for generation of dislocation increases as the crystallite size decreases [27]. Therefore, defect formed by fracturing of particles and reduction rate in crystallite size drops beyond 10 h.
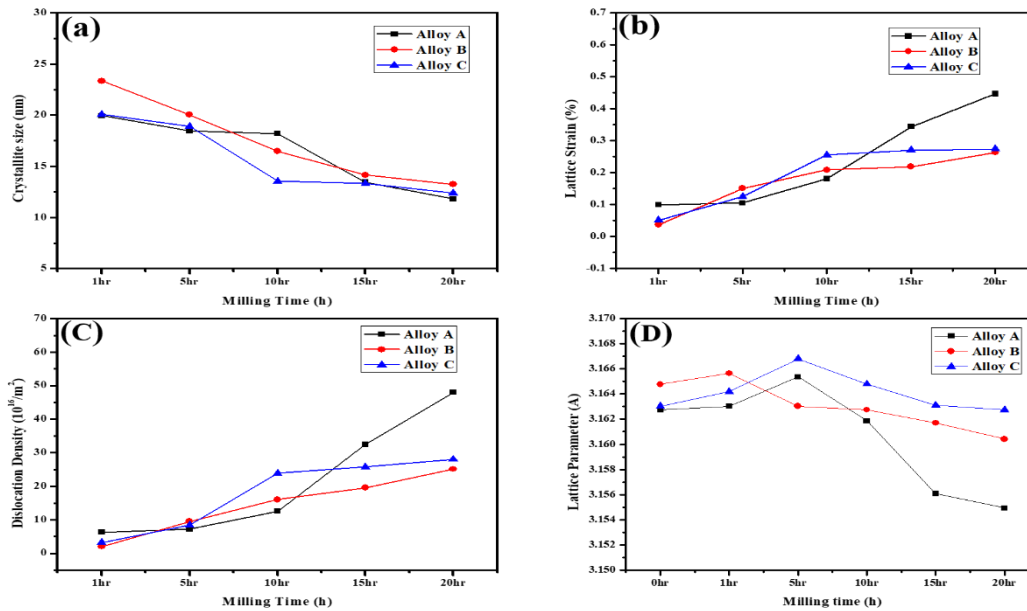

Fig.2. Variation of (a) crystallite size, (b) lattice strain, (c) Variation of dislocation density, (d) Variation of lattice parameter at different milling time for alloy A through C.

3.1.3. Dislocation density analysis.

The dislocation density of the milled powder (A through C) shows a sharp increasing trend with the increasing milling time to 10 h and its increases moderately beyond 10 h to 20 h of milling owing to considerable crystallite size reduction and crystal defect formation during initial mechanical milling. Maximum dislocation density of $47.98 \times 10^{16}/m^2$ is found in alloy A at 20 h of milling, this is attributed to higher W content in alloy A resulting in more brittleness resulting in higher fracturing of particles and defects formation which leads to higher dislocation compared to alloy (B and C). Fig. 2(c) shows the variation of dislocation density at different milling time [28].

3.1.4. Lattice parameter analysis.

The lattice parameter is evaluated by using Nelson–Riley extrapolation method [26].

$$\frac{cos^2\theta}{sin\theta} + \frac{cos^2\theta}{\theta} \qquad (3)$$

In this method, we selected four peaks of W of high intensity and value of Nelson-Riley function (equation 3) was evaluated for all those four peaks. After linearly fitting function

values, then function fitting line was extrapolated such that it cuts Y- axis. The value at which line cuts Y-axis is the precise value of corresponding lattice parameter at that hour of milling. Fig. 2(d) shows lattice parameter of W in all alloys (A through C) initially increases followed by contraction trends. This is attributed to the exertion of negative hydrostatic pressure in W lattice due to deformation arising from high energy during mechanical allying. Similar phenomenon of Nb lattice during mechanical milling of pure Nb was reported by Pabi et al. [29]. Contraction beyond 10 h of milling in W alloys (A through C). Patra et al. [30] and S. Telu et al. [31] have reported the contraction of W lattice in W-Cr and W-Ni-Mo alloys during mechanical milling. Atomic radius of W (0.193 nm) which is higher than both Ni (0.149 nm) and Mo (0.190nm) leads to reduction in lattice parameter of W after 10 h of milling [32]. Table 2 shows the four peak position (2θ) and d spacing of 20 h mechanically milled alloy (A through C) as evaluated from XRD pattern. Reduced d spacing indicates the increase in W lattice disorder (contraction in lattice parameter) for a specific plane.

Table 2

Peak position and d spacing of 20 h mechanically milled alloy A through C.

Alloy	Plane (hkl)	Peak position (°)	d spacing (Å)
A	110	47.095	2.23903
	200	68.824	1.5828
	211	87.556	1.29289
	220	106.19	1.118
B	110	47.059	2.23966
	200	68.871	1.58299
	211	87.694	1.2923
	220	106.2	1.11857
C	110	47.162	2.236
	200	68.902	1.57934
	211	87.755	1.29056
	220	106.15	1.118

3.1.5 SEM study of milled powder

Fig. 3 displayed the morphology and particle size of alloy C with increasing milling time from 0 h to 20 h respectively. The particles are coarser and irregular shape before the initiation of milling (0 h) (Fig. 3(a)). During milling the particles are work hardened and subsequently flattened and fractured with increasing milling time. Generation of new surfaces during rapture leads to agglomeration (cold working) after 5 h of milling, which tends to forms new particles with increased average particle size (Fig. 3(b-c)). Beyond 10 h of milling due to cold worked finer particles size, the milling energy required for rapturing and fragmenting the

powder particles increases. Therefore it is difficult to rapture the cold worked particle after 10 h of milling time. The uneven shaped powder particles are converted to both elongated and flake shape morphology at 10 h of milling and ultrafine morphology at 20 h (Fig. 3(e)) of milling. Fig. 4 shows the EDS pattern for mechanically milled powder of alloy C at 20 h. Table 3 shows the compositional distribution of 20 h mechanically milled alloy, which is non-homogeneous at 20 h of milling against the initial powder combination.
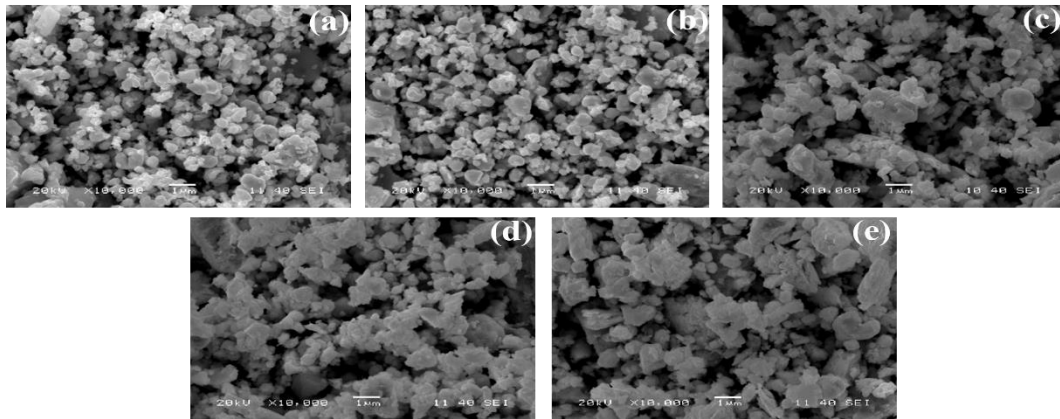

Fig. 3. SEM micrograph of powder morphology of alloy C at various milling intervals: (a) 0 h, (b) 5 h, (c) 10 h, (d) 15 h and (e) 20 h.

Table 3

EDS analysis of alloy C after 20 h of milling.

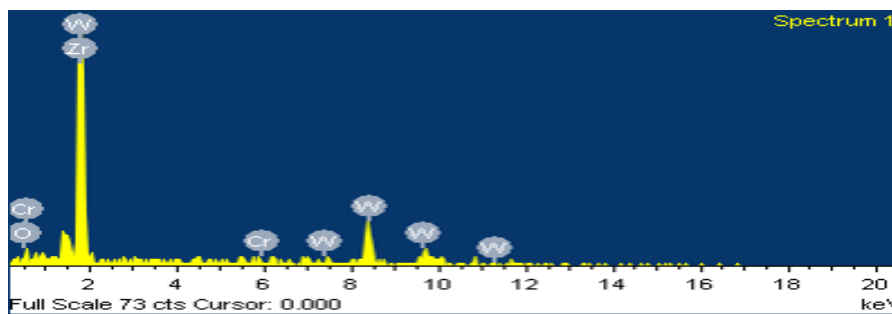| Element	Composition	
	[wt.%]	[at.%]
O	9.83	53.68
Cr	1.31	2.20
Zr	3.91	3.75
W	84.95	40.37

Fig. 4. EDS pattern of alloy C at 20 h

3.1.6. Particle size analysis

Powder morphology changes continuously during mechanically milling. The powder mixture was measured by Malvern particle size analyzer. Fig. 5(a). Shows the particle size distribution of milled powder at different milling time. It is evident from the figure that the average particle size has been increased at initial few hours to an extent then reduced to the final hours of milling. There was evidence of welding, as the particle size increased during the initial stages of milling. It should be mentioned that size morphology corresponding to individual milled powder of W alloys show evidence of growth in particle size. The minimum average particle size of 321.6nm was observed in alloy C.

3.1.7 Differential scanning calorimetric study

Fig. 5(b) shows the Differential Scanning Calorimetric (DSC) of the 20 h milled powder of alloy A through C has been carried out at heating rates (10 K/min) up to 1273 K (1000 °C) in argon atmosphere. It is evident from the peak that the recrystallization peak for alloy C is higher among all alloy. DSC of alloy C shows large peak broadening due to crystal growth and crystallization of amorphous mechanically milled powder during heating. Increment in the recrystallization temperature with heating rate is related with progress in plasticity attributable to easing of internal stress by heating. The recrystallization temperature of alloys (A through C) comparably less than pure W (1500 °C) owing to the effect of addition of alloying elements like Zr and Cr_2O_3 [33].

3.1.8 Calculation of flowability

The flowability of the 20 h milled powder evaluated by calculating the angle of Repose value. Where alloys A had the least angle of Repose 25.029°, thereby it holds the highest excellent flow character and least agglomeration of powder particles after 20 h of milling and it is also evident from the fig. 5(a) that alloy A shows the larger particles size, low surface area and high density due to maximum content of W powder. Table 4 shows the flowability of the 20 h milled powder.
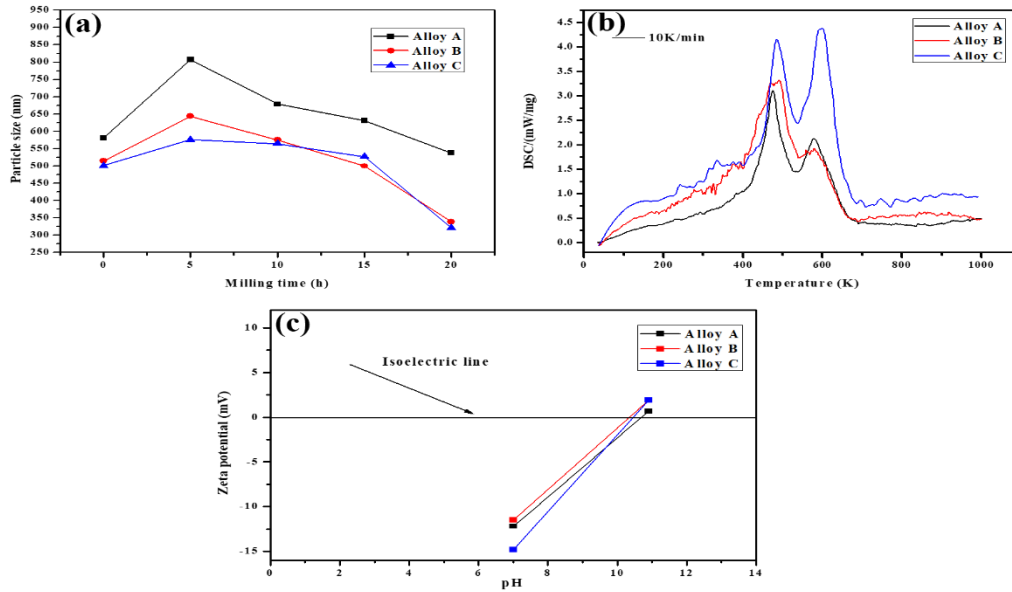
Fig. 5. Variation of (a) average particle size, (b) DSC plot at heating rate of 10 K/min, (c) zeta potential of alloy (A through C) at different milling time.

Table 4

Flowability analysis of (Alloy through C) after 20 h of milling.

Alloy	Flowability (Angle of Repose 'α') (°)
A	25.029
B	25.290
C	28.630

3.1.9 Dispersion stability of W-Zr-Cr$_2$O$_3$ ultrafine particle in base fluid

The stability of the dispersion was calculated by measuring zeta potential values of milled powder dispersed in de-ionized water. Dilute fraction of alloy suspension was selected for zeta potential measurement. The values of zeta potential ζ can be evaluated using the Helmholtz-Smoluchowski equation [34].

$$\zeta = \frac{\mu \cup}{\varepsilon} \tag{4}$$

where $\cup$= electrophoretic mobality, μ = viscosity and $\in$ is the dielectric constant of the liquid in the boundary.

The zeta potential is zero at a particular pH like in alloy B (at pH 10.2) touching the isoelectric line as shown in Fig. 5(c). Therefore the dispersion is less stable as the force of

electrostatic repulsion between the particles in not sufficient to overcome the attraction force between the particles, thereby the coagulated particles cannot redisperse through mechanical force. As the pH increases by adding reacting reagent ammonium hydroxide (NH₄OH), then the particles tend to acquire less charge, hence the electrostatic repulsion force between the particles becomes less sufficient to prevent attraction and collision between particles caused by Brownian motion.

At pH 7 the zeta potential becomes higher; so the electrostatic repulsion force between particles in stronger, and with mechanical force coagulated particles can redisperse. Therefore the dispersion stability of alloy C is best at pH 7 corresponding to zeta potential values of -14.8 mV [35].

5. Summary

Nanostructured W-Zr-Cr_2O_3 alloy powders are prepared with variation in composition by mechanically alloying for 20 h. The dissolution of Zr and Cr_2O_3 in W shows enhanced solid solubility in XRD analysis. Minimum crystallite size of 11.8 nm and the maximum lattice strain and dislocation density of 0.44% and $47.98 \times 10^{16}/m^2$ was achieved in $W_{98.5}Zr_{0.5}(Cr_2O_3)_1$(alloy A) at 20 h milling time due to presence of high surface energy associated with dispersed Cr_2O_3 particles which are in nanometer. The lattice parameter of all alloys first shows an increasing trend due to exertion of hydrostatic stress by nano-crystals and decreasing trend at 20 h of milling due to formation of solid solution. Non-uniform and coarser particles at 0 h of milling have been converted to both elongated and flake shape with the uniform size distribution of particles at 20 h of milling for all alloys. $W_{98.5}Zr_{0.5}(Cr_2O_3)_1$(alloy A) holds the highest excellent flow character and least agglomeration of powder particles. At 20 h of milling $W_{98}Zr_1(Cr_2O_3)_{(1)}$ (alloy C) shows average smallest particle size of 321.6nm and maximum dispersed stability at pH 7 corresponding to zeta potential values of -14.8 mV.

References

[1]   E. Lassner, W.D. Schubert, Tungsten-properties, Chemistry, Technology of the Element, Alloys, and Chemical Compounds, Kluwer Academic/Plenum Publishers, New York, 1999, pp. 255-268 (and 85).

[2]   C. Suryanarayana, Prog. Mater. Sci., 46 (2001), pp. 1-184.

[3]   D.K. Kolia, G. Agnihotri, R. Purohit, Procedia Materials Science, 6 (2014), pp. 567-589.

[4]   P. Norajitra, L.V. Boccaccini, A. Gervash, R. Giniyatulin, N. Holstein, T. Ihli, G. Janeschitz, W. Krauss, R. Kruessmann, V. Kuznetsov, A. Makhankov, I. Mazul, A. Moeslang, I. Ovchinnikov, M. Rieth, B. Zeep J. Nucl. Mater. 367-370 (2007), pp. 1416-1421.

[5]   H. Kurishita, S. Kobayashi, K. Nakai, T. Ogawa, A. Hasegawa, K. Abe, H. Arakawa, S. Matsuo, T. Takida, K. Takebe, M. Kawai, N. Yoshida J. Nucl. Mater, 377 (2008), pp. 34-40.

[6]   H. Kurishita, Y. Amano, S. Kobayashi, K. Nakai, H. Arakawa, Y. Hiraoka, T. Takida, K. Takebe, H. Matsui J. Nucl. Mater. 367–370 (2007), p. 1453.

[7]   J.L. Johnson, Sintering of refractory metals, in: Z.Z. Fang (Ed.), Sintering of Advanced Materials-Fundamentals and Processes, Woodhead Publishing, Cambridge (UK) (2010), pp. 357-380.

[8]   H. Kurishita, S. Kobayashi, K. Nakai, T. Ogawa, A. Hasegawa, K. Abe, H. Arakawa, S. Matsuo, T. Takida, K. Takebe, M. Kawai, N. Yoshida, J. Nucl. Mater. 377 (2008) 34–40.

[9]   H. Kurishita, Y. Amano, S. Kobayashi, K. Nakai, H. Arakawa, Y. Hiraoka, T. Takida, K. Takebe, H. Matsui, J. Nucl. Mater. 367–370 (2007) 1453.

[10] Y. Zhang, A.V. Ganeev, J.T. Wang, J.Q. Liu, I.V. Alexandrov, Mater. Sci. Eng. A 503 (2009) 37–40.

[11] L.J. Kecskes, K.C. Cho, R.J. Dowding, B.E. Schuster, R.Z. Valiev, Q. Wei, Mater. Sci. Eng. A. 467 (2007) 33–43.

[12] H. Kurishita, T. Kuwabara, M. Hasegawa, S. Kobayashi, K. Nakai, J. Nucl. Mater. 343 (2005) 318–324.

[13] Y. Kim, K.H. Lee, E.P. Kim, D.I. Cheong, S.H. Hong, Int. J. Refract. Met. Hard Mater. 27 (2009) 842–846.

[14] M. Rieth, B. Dafferner, J. Nucl. Mater. 342 (2005) 20–25.

[15] M.A. Yar, S. Wahlberg, H. Bergqivist, H.G. Salem, M. Johnsson, M.

Muhammed, J. Nucl. Mater. 412 (2011) 227–232.

[16] M.A. Yar, S. Wahlberg, H. Bergqvis, H.G. Salem, M. Johnsson, M. Muhammed, J. Nucl. Mater. 408 (2011) 129–135.

[17] A. Munoz, M.A. Monge, B. Savoini, M.E. Rabanal, G. Garces, R. Pareja, J. Nucl. Mater. 417 (2011) 508–511.

[18] I. Wesemann, W. Spielmann, P. Heel, A. Hoffmann, Int. J. Refract. Met. Hard Mater. 28 (2010) 687–691.

[19] Z.M. Xie, R. Liu, Q.F. Fang, Y. Zhou, X.P. Wang, C.S. Liu, J. Nucl. Mater. 444 (2014) 175–180.

[20] R. Liu, Z.M. Xie, T. Hao, Y. Zhou, X.P. Wang, Q.F. Fang, C.S. Liu, J. Nucl. Mater. 451, (2014) 35–39.

[21] B. Cullity, Elements of X-Ray Diffraction, second ed. Addison Wesley, Philippines, 1978 86–88.

[22] G.K. Williamson, W.H. Hall, X-ray line broadening from filed aluminium and wol- fram, Acta Mater. 1 (1) (1953) 22–31.

[23] G.K. Williamson, Smallman, Dislocation densities in some annealed and cold-worked metals from measurements on the X-ray Debye-Scherrer spectrum, Philos. Mag. 1 (1) (1956) 34–46.

[24] R.E. Smallman, K.H. Westmacott, Stacking faults in face-centred cubic metals and al- loys, Philos. Mag. 2 (17) (1957) 669–683.

[25] Y.H. Zhao, H.W. Sheng, K. Lu, Microstructure evolution and thermal properties in nanocrystalline Fe during mechanical attrition, Acta Mater. 49 (2) (2001) 365–375.

[26] R. Jenkins, R.L. Snyder, Introduction to X-Ray Powder Diffractometry, J Wiley & Sons Inc, New York, 1996.

[27] M. Nuthalapati, S.K. Karak, J.D. Majumdar, A. Basu, Phase evolution and mechanical properties of Nano-TiO_2 dispersed Zr-based alloys by mechanical alloying and con- ventional sintering, Metall. Mater. Trans. A 45A (2014) 3748–3754.

[28] Y.H. Zhao, H.W. Sheng, K. Lu, Microstructure evolution and thermal properties in nanocrystalline Fe during mechanical attrition, Acta Mater., 49 (2) (2001), pp. 365-375.

[29] P.P. Chattopadhayay, P.M.G. Nambissan, S.K. Pabi, I. Manna, Polymorphic transfor- mation and lattice expansion in nanocrystalline niobium revealed by positron anni- hilation at grain boundary, Appl. Surf. Sci. 182 (2001) 308–312.

[30] A. Patra, S.K. Karak, S. Pal, Synthesis and characterization of $W_{80}Ni_{10}Mo_{10}$ alloy pro- duced by mechanical alloying, IOP Conf. Ser. Mater. Sci. Eng. 75 (012032) (2015) 1–6.

[31] S. Telu, A. Patra, M. Sankaranarayana, R. Mitra, S.K. Pabi, Microstructure and cyclic oxidation behavior of W–Cr alloys prepared by sintering of mechanically alloyed nanocrystalline powders, Int. J. Refract. Met. Hard Mater. 36 (2013) 192–194.

[32] V. Singh, Physical Metallurgy, first ed. Standard Publisher Distributor, New Delhi, 2002 63–64.

[33] A. Patra, R. Saxena, S.K. Karak, Combined effect of Ni and nano-Y_2O_3 addition on microstructure, mechanically and high temperature behaviour of mechanically alloyed W-Mo, Int. Journal of refactory Metals and Hard Materials 60 (2016) 131-146.

[34] Alice Sze, David Erickson, Liqing Ren, and Dongqing Li, Zeta-potential measurement using the Smoluchowski equation and the slope of the current–time relationship in electroosmotic flow, Journal of Colloid and Interface Science 261 (2003) 402–410.

[35] S. Samal, B. Satpati, D. Chaira, Production and dispersion stability of ultrafine Al-Cu alloy powder in base fluid, Journal of Alloys and Compounds 504S (2010) S389-S394.